

# Dynamical opacity-sampling models of Mira variables – II. Time-dependent atmospheric structure and observable properties of four M-type model series

M. J. Ireland,<sup>1,2,3\*</sup> M. Scholz<sup>1,4</sup> and P. R. Wood<sup>5</sup>

<sup>1</sup>*Sydney Institute for Astronomy (SfA), School of Physics, University of Sydney, NSW 2006, Australia*

<sup>2</sup>*Department of Physics and Astronomy, Macquarie University, NSW 2109, Australia*

<sup>3</sup>*Australian Astronomical Observatory, PO Box 296, Epping, NSW 1710, Australia*

<sup>4</sup>*Zentrum für Astronomie der Universität Heidelberg (ZAH), Institut für Theoretische Astrophysik, Albert-Ueberle-Str. 2, 69120 Heidelberg, Germany*

<sup>5</sup>*Research School for Astronomy and Astrophysics, Australian National University, Canberra, ACT 2600, Australia*

Accepted 2011 July 18. Received 2011 July 18; in original form 2011 May 22

## ABSTRACT

We present four model series of the CODEX dynamical opacity-sampling models of Mira variables with solar abundances, designed to have parameters similar to *o* Cet, R Leo and R Cas. We demonstrate that the CODEX models provide a clear physical basis for the molecular shell scenario used to explain interferometric observations of Mira variables. We show that these models generally provide a good match to photometry and interferometry at wavelengths between the near-infrared and the radio, and make the model outputs publicly available. These models also demonstrate that, in order to match visible and infrared observations, the Fe-poor silicate grains that form within 3 continuum radii must have small grain radii and therefore cannot drive the winds from O-rich Mira variables.

**Key words:** stars: AGB and post-AGB – stars: atmospheres – stars: mass-loss – stars: variables: general.

## 1 INTRODUCTION

Asymptotic giant branch (AGB) stars represent the final fusion-powered stage in the evolution of solar-type stars, and the engine by which the vast majority of the material in our Galaxy is recycled from stars back to the interstellar medium (Gail 2003). Mira variables represent the final stage in the AGB evolution before they become dust-enshrouded and difficult to observe. They are so bright in the infrared that they can be used as competitive extragalactic distance indicators and probes of star formation history (Rejkuba 2004; Menzies et al. 2010). They are also unique amongst stellar classes in their opportunity for detailed observations: light curves that differ in shape and amplitude in different bandpasses, photospheres that show different sizes and structure as a function of wavelength, velocity-resolved motions and complex spectra.

The observational literature on Mira variables is very extensive, as partly detailed in Section 4. In order to make sense of these observations, comprehensive models are required that link physical parameters to pulsation, and pulsation to observed properties and mass loss. The previous generation of models (e.g. Höfner et al. 1998; Hofmann, Scholz & Wood 1998) suffered from grey or mean-opacity-like approximations in their radiative transfer codes, so they were not ideally suited for interpreting many observed properties,

for example visible brightness or high-resolution spectroscopy. The next generation of models (Upsalla: Höfner et al. 2003, CODEX: Ireland, Scholz & Wood 2008, hereafter Paper I) are better suited for modern observational comparisons, but extensive grids have not yet been produced, both because of solvable but difficult computational issues and the lack of a clear calibration for model parameters.

Here we present four physical model series for M-type Mira variables, as a first step in tuning and testing the CODEX models to derive physical parameters of Mira variables from observations, and to gain physical insight into the dominant physical processes in Mira-variable atmospheres. Observational predictions including predictions for infrared interferometry of the model series are made available online so that new observations can easily be compared to these models.

One of these model series has parameters based on *o* Cet, one based on R Leo and two are based on R Cas with different assumptions. For all models, only the pulsation period is guaranteed to match observations, and in this paper we aim to examine the other model outputs in order to more closely target model series to real stars in future papers. The model construction is described in Paper I: they begin with input parameters of mass, luminosity and composition, with three other free parameters being microturbulent velocity, mixing length ( $\alpha_m$ ) and turbulent viscosity ( $\alpha_v$ ). Pulsation is self-excited (i.e. it occurs spontaneously), and the temperature of all layers is calculated by solving the conservation of energy equation via a detailed opacity-sampling method.

\*E-mail: michael.ireland@mq.edu.au

Details of the parameter choices for the model series are given in Section 2, along with the basic comparison of the model light curves to observations. Model predictions for spectra, in particular the effect of extension on spectra, are tested in Section 3, and the models are compared to observations of *o* Ceti including infrared and radio interferometry in Section 4. In Section 6, we compare the model structures to previously published ad hoc molecular shell papers, and in Section 7 we discuss the mass-loss rates of the models and the driving mechanisms. In Section 5 we discuss the effect of input parameters on the models, and the possibility for better calibrating the input parameters so that, e.g., the mass of individual Miras could be inferred from models. Finally, in Section 8 we conclude and discuss plans for future work.

## 2 MODEL PARAMETERS AND DESCRIPTION

A detailed description of the model construction is given in Paper I. Briefly, the models consist of self-excited grey models that determine the atmospheric pressure stratification and luminosity. The temperature profile is then re-iterated using an opacity-sampling code with 4300 wavelength points, assuming radiative and local thermodynamic equilibrium. Dust formation follows Ireland & Scholz (2006), except that we drop the Rayleigh approximation, instead replacing it by a smooth fit to the Mie approximation of spherical grains, weighting the Rayleigh scattering by

$$\sigma_M(a, \lambda) = \sigma_R(a, \lambda) \left( 1 + 4.5 \left( \frac{a}{\lambda} \right)^4 \right)^{-1}, \quad (1)$$

where  $a$  is the grain radius,  $\lambda$  the wavelength of radiation,  $\sigma$  the scattering cross-section and  $\sigma_R$  the scattering cross-section in the Rayleigh approximation. This cross-section  $\sigma_M$  is the total cross-section weighted by  $(1 - \mu)$ , where  $\mu$  is the impact parameter. This weighting ensures that the radiative acceleration on dust is correct in the presence of forward-scattering.

The choice of free parameters was only briefly discussed in Paper I in the context of the *o*54 model series, based on the parameters of the prototype Mira variable *o* Ceti. The input parameters for all four model series presented here are given in Table 1, and the reasons for their choice are given in Sections 2.1–2.4.

The behaviour over  $10^4$  d of each non-linear pulsation model series is shown in Figs 1–4. As each model series runs for many cycles, we chose only a few typical cycles for a detailed examination. In each of these cycles,  $\sim 10$  representative models were extracted and their velocity and pressure structures used as input to the model atmosphere code which, after temperature iteration, give spectra and centre-to-limb variation (CLV) for the models. The cycles during which models were extracted are shown as shaded regions in Figs 1–4 and the actual models extracted are shown as circles in the top panels of these figures. The instantaneous physical parameters and shock-front locations for the chosen models are given in

**Table 1.** Parameters of four model series. The mass  $M$ , luminosity  $L$ , metallicity  $Z$ , mixing-length parameter  $\alpha_m$  and turbulent viscosity parameter  $\alpha_\mu$  are input parameters, and the parent-star radius  $R_p$  and period  $P$  are derived parameters.

Name	$M$	$L$	$Z$	$\alpha_m$	$\alpha_\mu$	$R_p$	$P$	$P_{\text{linear}}$
<i>o</i> 54	1.1	5400	0.02	3.5	0.25	216	330	261
R52	1.1	5200	0.02	3.5	0.25	209	307	243
C50	1.35	5050	0.02	2.0	0.24	291	427	408
C81	1.35	8160	0.02	3.5	0.32	278	430	374

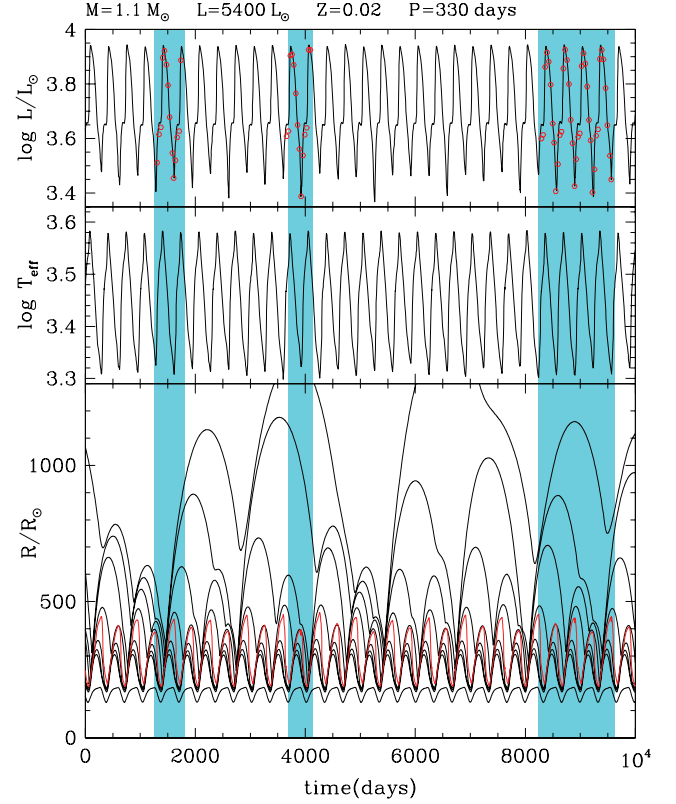


**Figure 1.** The luminosity (top panel), effective temperature (middle panel) and the radii of a representative selection of mass zones (bottom panel) plotted against time for model *o*54. The red line in the bottom panel shows the position of the point where the grey approximation optical depth  $\tau_g = \frac{2}{3}$ .  $T_{\text{eff}}$  in the middle panel is here defined as the temperature where  $\tau_g = 2/3$ , which is close to the effective temperature  $\propto (L/R^2)^{1/4}$  of the non-grey atmospheric stratification. The shaded regions show the time intervals in which models were selected for detailed atmospheric model computation. The selected models are circled in the top panel. The mass, luminosity, metallicity and period of the non-linear pulsation model are shown at the top of the plot.

Tables 3–8. We note that the model radius is defined in these tables as the radius where the Rosseland optical depth is unity, and the effective temperature is defined by this radius.

For all four model series, we assume solar element abundances from Grevesse, Noels & Sauval (1996). This is near the mean abundance observed for stars in the solar vicinity with ages of  $3\text{--}6 \times 10^9$  yr (Edvardsson et al. 1993). Our red giant model with mass  $1.35 M_\odot$  has an age of  $\sim 3 \times 10^9$  yr and the red giant model with mass  $1.1 M_\odot$  has an age of  $\sim 6 \times 10^9$  yr according to the isochrones of Girardi et al. (2000). However, as shown by Edvardsson et al. (1993), there is a scatter in  $[\text{Fe}/\text{H}]$  from about  $-0.5$  to  $+0.3$  for stars of this age, so that the Mira stars we are aiming to model could have somewhat different abundances to those we have adopted.

The adopted value for the mixing length in units of pressure scale-height for the *o*54, R52 and C81 series,  $\alpha_m = 3.5$ , is unusually high compared with models of more compact stars. However, this is not unreasonable, as detailed hydrodynamic calculations of stellar convection often suggest values for  $\alpha_m$  in the range 1–4 (see the parameter summary in Meakin & Arnett 2007). Decreasing the mixing length in models makes heat transport more difficult in the outer convective layers, causing the model star to expand. Therefore,

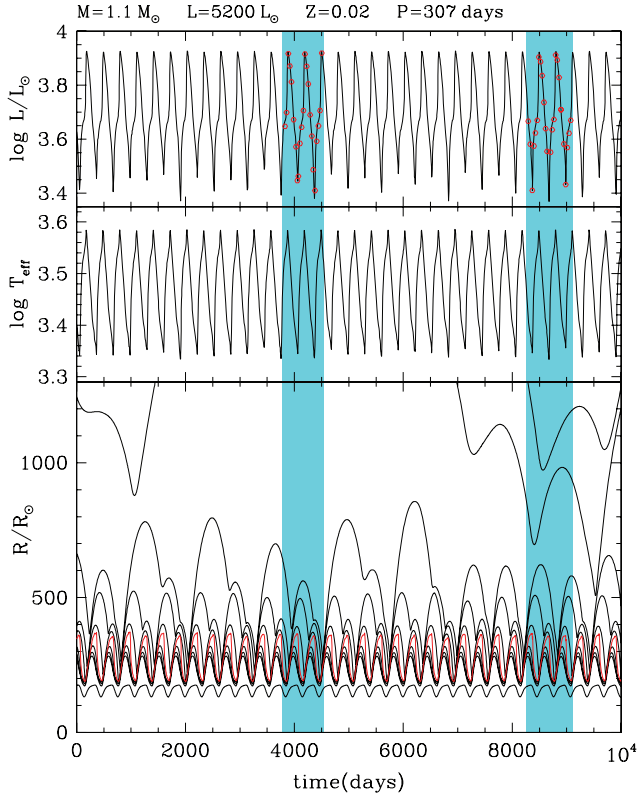


**Figure 2.** The luminosity and mass-zone positions in the R52 series, showing the locations of the phases chosen for detailed model computation.

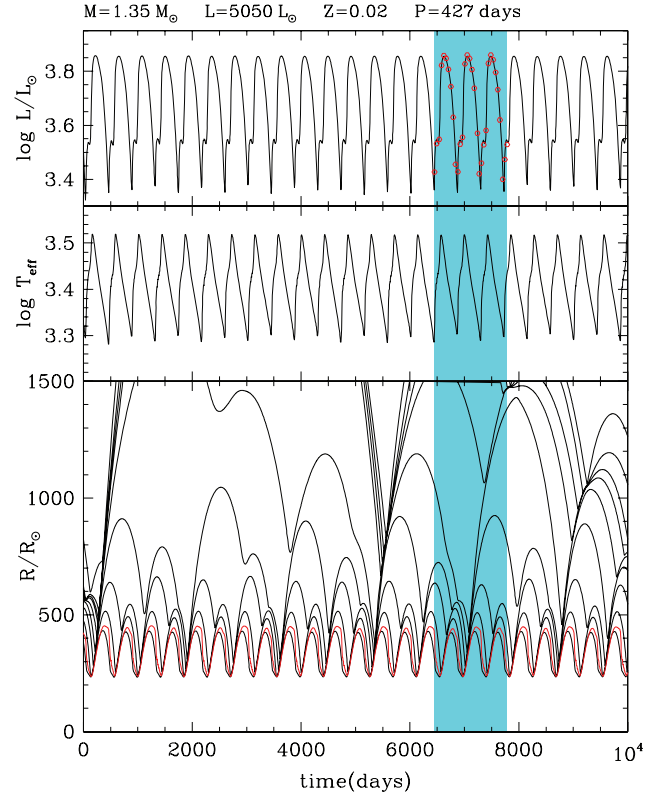


**Figure 4.** The luminosity and mass-zone positions in the C50 series, showing the locations of the phases chosen for detailed model computation.

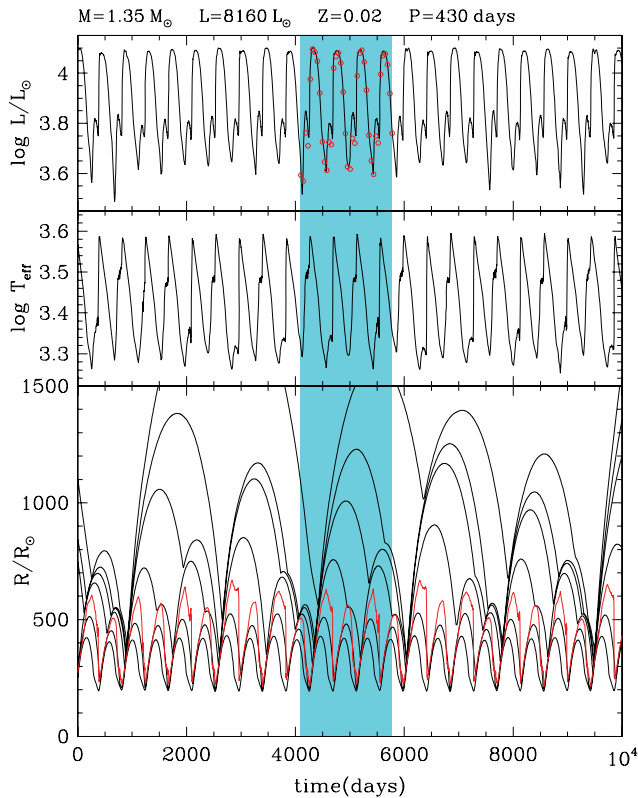


**Figure 3.** The luminosity and mass-zone positions in the C81 series, showing the locations of the phases chosen for detailed model computation.

mixing length has been used by us as a way to produce the correct period, given a luminosity  $L$ . However, this procedure is always ambiguous for a given field Mira, because the distance and hence  $M$  are always uncertain by  $\sim 10$  per cent or more.

The value of  $\alpha_v$  can be adjusted to give the correct pulsation amplitude. Alternatively, within limits,  $M$  can be adjusted to give the correct pulsation amplitude. Thus far, in our models series, we have assumed values of  $M$  based on e.g. typical masses as a function of period and then used  $\alpha_v$  to tune the pulsation amplitude. By comparing these model series with observations, we aim to develop preferred values for  $\alpha_m$  and  $\alpha_v$ , or at least a preferred prescription for choosing  $\alpha_m$  and  $\alpha_v$  as a function of the physical input parameters  $M$ ,  $L$  (a proxy for evolutionary state along the AGB) and  $Z$ .

Although our models have been generally based on the stars  $\alpha$  Cen, R Leo and R Cas, there are a range of parameters that are consistent with these Miras, and a detailed comparison with observations will inevitably reveal where the differences lie. In the following section, we aim to discuss the chosen parameters for each model series, compare predicted light curves to observed light curves and draw preliminary conclusions as to whether changes to physical input parameters could improve model fits. We choose the  $V$ ,  $J$  and  $K$  band for comparison to observations:  $V$  band because of the wealth of observational data, and  $J$  and  $K$  because the model predictions are most reliable in these bandpasses. For this comparison, we add 0.5 mag to the predicted  $V$ -band fluxes to account for non-LTE effects as computed in the models at selected phases in Paper I, where the correction needed varies between 0.3 and 1.0 mag.

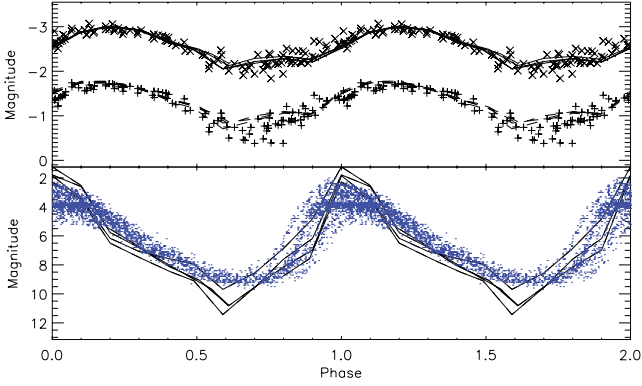


**Figure 5.** Light curves of the o54 series in *J*, *K* and *V* bands compared with observations of *o* Cet by Whitelock et al. (2000) and the Association Française des Observateurs d'Etoiles Variables (AFOEV).

### 2.1 o54 5400 $L_{\odot}$ series

The 5400  $L_{\odot}$  model series for *o* Cet ( $P = 332$  d) has model parameters chosen to match the luminosity obtained from the *J* and *K* photometry of Whitelock, Marang & Feast (2000) and the Knapp et al. (2003) revised *Hipparcos* parallax. The mass of  $1.1 M_{\odot}$  was adopted since an analysis of the Galactic scaleheight of Mira variables by Jura & Kleinmann (1992) suggests a mass of  $\sim 1.1 M_{\odot}$  for Mira variables with periods from 300 to 400 d, while a study of the population of Miras by Wyatt & Cahn (1983) gives a progenitor mass estimate of  $1.18 M_{\odot}$  for *o* Cet. We give this model series the designation o54.

Fig. 5 shows the light curves derived from four cycles of the o54 model series between times 8000 and  $10^4$  d in Fig. 1. To fit the *K*-band maximum flux of *o* Cet, the model needs to be placed at a distance of 107 pc. This corresponds to a parallax of 9.3 mas, consistent within  $2\sigma$  of the latest *Hipparcos* value of  $10.91 \pm 1.22$  mas from van Leeuwen (2007).

The models fit the general light-curve shape and amplitude, but they are  $\sim 0.1$  mag too blue in *J* – *K* colour, too blue in *V* – *K* by  $\sim 1$  mag (hence too bright in *V* near maximum by  $\sim 1$  mag), and these four cycles do not reproduce the cycle-to-cycle scatter in *J* and *K* magnitudes near minimum.

We also computed models for more compact atmosphere cycles (between times 1000 and 2000 d in Fig. 1) and more extended atmosphere cycles (between times 3500 and 4300 d), but *J*, *H* and *V* fluxes were not noticeably different. The atmospheric structures for the various models are shown in Fig. 1. The consistently blue *J* – *K* and *V* – *K* colours suggest that  $T_{\text{eff}}$  is too high in the model (see Section 5 for more discussion).

Although the basic model properties ( $L$ ,  $R$ ,  $T_{\text{eff}}$ ) and the near-continuum fluxes are similar from cycle to cycle, high-layer observational features differ depending on the upper atmosphere structure. The reason for this can be seen in Tables 2–4, where upper-layer shock-front positions are not repeatable from cycle to cycle. For example, in Table 2, at phase  $-0.2$ , the upper strong shock from a previous cycle is at  $2.82 R_p$ . Exactly one cycle later, at phase 0.8, the upper shock has just merged with a lower shock at  $1.82 R_p$ , as shown by the  $\Rightarrow$  symbol in Table 2.

### 2.2 R52 5200 $L_{\odot}$ series

The period of R Leo is slightly shorter than that of *o* Cet, and we chose to model R Leo with a model identical to the *o* Cet model, but with a luminosity reduced to match the smaller period (310 versus

**Table 2.** Parameters of the extended o54 cycle, including the position of the shock fronts. The arrows ( $\Rightarrow$ ) indicate the merging of two shock fronts.

Model	Phase	$L$ ( $L_{\odot}$ )	$R$ ( $R_p$ )	$T_{\text{eff}}$ (K)	S1 ( $R_p$ )	S2 ( $R_p$ )	S3 ( $R_p$ )
260820	−0.20	4050	0.90	3299	2.82	0.91	
260960	−0.10	4240	0.85	3434	2.85	0.87	
261140	0.00	8013	0.98	3761	2.86	0.99	
261320	0.10	8102	1.20	3398	2.87	1.28	
261460	0.19	7420	1.34	3154	2.83	1.50	
261620	0.31	5830	1.41	2898	2.74	1.70	
261740	0.40	4462	1.42	2697	2.64	1.82	
261860	0.50	3640	1.34	2640	2.47	1.91	
261940	0.60	2440	1.40	2333	2.31	1.93	
262160	0.70	3450	0.97	3055	2.07	1.89	0.97
262360	0.80	4110	0.90	3325	$\Rightarrow$	1.82	0.90
262600	0.90	4355	0.85	3462		1.74	0.86
263160	1.00	8428	0.99	3786		1.61	1.01
263740	1.10	8420	1.20	3439		$\Rightarrow$	1.37

**Table 3.** Parameters of the compact o54 cycle, including the position of the shock fronts.

Model	Phase	$L$ ( $L_{\odot}$ )	$R$ ( $R_p$ )	$T_{\text{eff}}$ (K)	S1 ( $R_p$ )	S2 ( $R_p$ )	S3 ( $R_p$ )
248480	−0.30	3243	0.99	2982	2.03	0.99	
248680	−0.20	4122	0.90	3312	2.02	0.91	
248900	−0.10	4379	0.86	3450	1.99	0.87	
249240	0.00	7870	0.95	3793	1.92	0.97	
249960	0.10	8358	1.18	3458	1.80	1.29	
250360	0.21	7432	1.34	3152	$\Rightarrow$	1.69	
250400	0.29	6239	1.39	2960		2.10	
250420	0.38	4768	1.41	2749		2.42	
250440	0.53	3520	1.33	2628		2.96	
250460	0.60	2847	1.32	2497		3.18	1.13
250640	0.70	3305	0.99	2990		3.46	0.99
250820	0.80	4019	0.91	3287		3.74	0.91
250980	0.90	4238	0.85	3436		4.01	0.86
251160	1.00	7713	0.96	3768		4.42	0.97

332 d). Miras typically also have reduced masses at reduced periods (Jura & Kleinmann 1992), but we chose not to reduce the mass so as to see the differential influence of luminosity alone (Wyatt & Cahn 1983 give a mass of  $1.04 M_{\odot}$  for R Leo). The model has a luminosity derived by assuming R Leo was at a distance of 110 pc, corresponding to a parallax of 9.1 mas, again consistent with the van Leeuwen (2007) value of  $14.03 \pm 2.65$  mas within  $2\sigma$ .

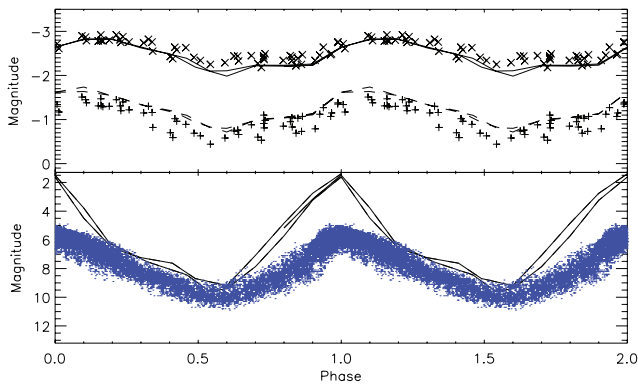
It is clear in Fig. 6 that this model is too blue to be an effective model for R Leo in both *V* – *K* and *J* – *K* colours, and has a visual amplitude much larger and a *K* amplitude slightly larger than R Leo. The amplitude of the R Leo model is slightly smaller than the amplitude of the *o* Cet model due to the reduced luminosity. This luminosity change by itself is not enough to explain the different visual amplitudes of the real R Leo and *o* Cet. It is possible that these two stars have different metallicity (i.e. the redder colours of R Leo could be because it has a higher metallicity). A difference in mass is also possible, with a compensating change in luminosity within that allowed by the parallax error to retain the same period.

Like the o54 series, we computed an extended sub-series (day numbers 3600–4500 in Fig. 2) and a compact sub-series (day numbers 8200–9100 in Fig. 2). The compact sub-series had its detailed radiative transfer model truncated at  $4 R_p$ , because the very



**Table 4.** Parameters of the four-cycle continuous phase coverage  $\phi 54$  cycle, including the position of the shock fronts.

Model	Phase	$L$ ( $L_{\odot}$ )	$R$ ( $R_p$ )	$T_{\text{eff}}$ (K)	S1 ( $R_p$ )	S2 ( $R_p$ )	S3 ( $R_p$ )	S4 ( $R_p$ )	S5 ( $R_p$ )	S6 ( $R_p$ )
285180	-0.20	3979	0.92	3263	3.54	0.92				
285320	-0.11	4107	0.86	3397	4.06	0.87				
285500	0.00	7288	0.93	3769	4.21	0.94				
285700	0.10	8236	1.17	3468	4.36	1.22				
285860	0.20	7623	1.33	3189	4.52	1.47				
285980	0.31	6270	1.40	2952		1.70				
286060	0.41	4513	1.43	2692		1.87				
286100	0.49	3845	1.40	2614		1.95				
286140	0.59	2548	1.53	2258		2.02				
286320	0.70	3204	1.00	2959		2.00	1.00			
286520	0.80	4092	0.91	3291		1.93	0.92			
286700	0.90	4218	0.86	3415		1.83	0.87			
287000	1.00	7188	0.93	3755		1.64	0.94			
287560	1.10	8431	1.17	3487		1.38	1.25			
287740	1.20	7734	1.32	3204	$\Rightarrow$		1.62			
287820	1.30	6304	1.40	2963			1.95			
287880	1.40	4658	1.43	2720			2.18			
287940	1.51	3820	1.38	2629			2.38			
287980	1.61	2661	1.47	2326			2.52	1.13		
288140	1.70	3342	1.00	2984			2.61	1.00		
288320	1.80	4034	0.91	3279			2.67	0.92		
288460	1.90	4159	0.86	3407			2.71	0.87		
288620	2.00	7340	0.93	3770			2.71	1.37		
288820	2.10	8170	1.17	3461			2.71	1.22		
289020	2.20	7495	1.32	3181			2.69	1.46		
289240	2.30	6174	1.40	2948			2.66	1.66		
289440	2.40	4655	1.42	2730			2.63	1.80		
289620	2.49	3918	1.36	2671			2.46	1.91		
289740	2.59	2525	1.42	2336			2.26	1.97		
289920	2.70	3064	0.99	2932			$\Rightarrow$	1.99	0.99	
290120	2.80	4073	0.91	3290				2.01	0.92	
290360	2.90	4301	0.86	3434				2.08	0.87	
290740	3.00	7795	0.95	3796				1.97	0.96	
291500	3.10	8412	1.17	3474				2.06	1.29	
291740	3.19	7759	1.32	3210				$\Rightarrow$	1.65	
291800	3.31	6097	1.40	2935					2.19	
291820	3.41	4451	1.43	2688					2.55	
291840	3.55	3438	1.40	2544					3.07	
291860	3.61	2813	1.35	2469					3.24	1.13

**Figure 6.** Light curves of the R52 series in the extended cycle in  $J$ ,  $K$  and  $V$  bands compared with observations by Whitelock et al. (2000) and the AFOEV.

low density in the outer layers ( $< 10^{-15} \text{ g cm}^{-3}$ ) had extremely low opacity and the models had outer-layer physical conditions outside the range where our equation of state was valid. Again, the  $V$ ,  $J$  and  $K$  fluxes were similar in each case (only the extended sub-series is displayed).

### 2.3 C81 8160 $L_{\odot}$ series

With the same input physics as the  $\alpha$  Ceti models, we attempted to create a longer period series appropriate for the Mira variable R Cas ( $P = 430 \text{ d}$ ) by increasing the luminosity and mass. However, the model pulsation amplitude became much too large, requiring us to increase the  $\alpha_v$  parameter. The *Hipparcos* distance for R Cas in Whitelock, Feast & van Leeuwen (2008) would require the star to be very underluminous when compared with the mean solar-velocity period–luminosity (P–L) relationship of Whitelock et al. (2008) or the Large Magellanic Cloud (LMC) P–L relationship (e.g. Hughes & Wood 1990). For this model series, the luminosity of our model was derived by assuming R Cas falls on the mean solar-velocity P–L

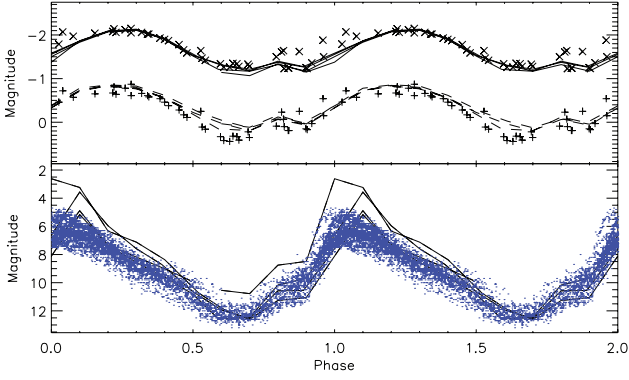


**Figure 7.** Light curves of the C81 series *J*, *K* and *V* bands compared with observations by Nadzhip et al. (2001) and the AFOEV.

relationship of Whitelock et al. (2008) and is at a distance of 204 pc, with a corresponding parallax of 4.9 mas, almost  $3\sigma$  from the van Leeuwen (2007) value of  $7.95 \pm 1.02$  mas. The mass adopted for R Cas is  $1.35 M_{\odot}$  as given by Wyatt & Cahn (1983).

The light curves of R Cas in the *V*, *J* and *K* bands are shown in Fig. 7, corresponding to day numbers  $\sim 4000$ – $5700$  chosen for detailed radiative transfer computation in Fig. 3. The *J* and *K* light curves of the model fit the observations quite well, while in all cycles where the near-maximum model was computed, the models are too bright in *V* near maximum light. The near-maximum continuum effective temperature is  $\sim 3800$  K in Table 8, corresponds to an M0 or M1 giant according to the temperature calibration of Fluks et al. (1994) and appears like an M2 giant in the TiO features as predicted by our model spectra. This is much too warm for R Cas which has a catalogued spectral type of M6–M10. Therefore, we are forced to conclude that  $T_{\text{eff}}$  is too high for this model.

## 2.4 C50 5050 $L_{\odot}$ series

As the  $8160 L_{\odot}$  model of R Cas was so clearly discrepant near maximum, and as the individual *Hipparcos* distance in Whitelock et al. (2008) would give a luminosity of only  $\sim 3770 L_{\odot}$ , we chose to construct a lower luminosity model. The luminosity was determined by fixing the mixing-length parameter which was decreased to a more standard value of  $\alpha_m = 2$ . The luminosity was then tuned to match the model period to that of R Cas. As usual, the turbulent viscosity parameter was then tuned to match the bolometric amplitude of R Cas and the model. The resulting luminosity ( $5050 L_{\odot}$ ) suggests that R Cas is at a distance of 166 pc with a corresponding parallax of 6.0 mas: this is now consistent with the *Hipparcos* value within  $2\sigma$ .

The near-maximum effective temperature of this model is now  $\sim 3250$  K, both consistent with an M6 spectral type from the calibration of Fluks et al. (1994) and providing a better match to the observed M6 spectra in Fluks et al. (1994) than either M5 or M7 spectra. It also has a *V* – *K* colour that matches that of R Cas (see Fig. 8).

## 2.5 Using the models

For each model phase in Tables 3–8, we provide the full model output.<sup>1</sup> Indeed, this output was already used by Woodruff et al. (2009) in advance of publication in order to compare the models

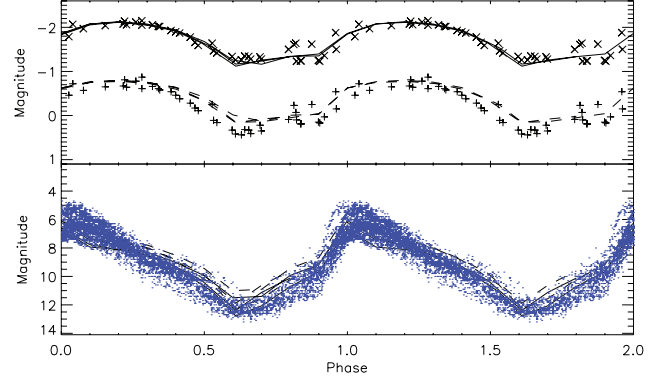


**Figure 8.** Light curves of the C50 series *J*, *K* and *V* bands compared with observations by Nadzhip et al. (2001) and the AFOEV.

**Table 5.** Parameters of the extended two cycles of the R52 series, including the position of the shock fronts.

Model	Phase	$L$ ( $L_{\odot}$ )	$R$ ( $R_p$ )	$T_{\text{eff}}$ (K)	S1 ( $R_p$ )	S2 ( $R_p$ )	S3 ( $R_p$ )	S4 ( $R_p$ )
360540	−0.20	4442	0.92	3411	2.02	0.93		
360760	−0.10	5000	0.91	3535	1.94	0.92		
361180	0.00	8266	1.06	3696	1.79	1.11		
361720	0.10	7425	1.24	3338	1.57	1.40		
361860	0.19	6491	1.33	3118	⇒	1.71		
361900	0.32	4700	1.36	2844		2.10		
361920	0.46	3729	1.25	2793		2.38		
361940	0.54	2795	1.15	2714		2.51		
362020	0.60	2901	1.06	2851		2.58	1.06	
362200	0.70	3837	0.96	3209		2.69	0.97	
362380	0.80	4405	0.92	3400		2.79	0.94	
362560	0.90	5083	0.91	3545		2.81	0.92	
362780	1.00	8236	1.06	3704		2.87	1.10	
363000	1.10	7408	1.24	3337		2.93	1.37	
363180	1.20	6374	1.33	3097		2.89	1.59	
363380	1.30	4897	1.36	2870		2.92	1.77	
363540	1.41	4088	1.31	2797		2.81	1.91	
363600	1.49	3063	1.24	2674		⇒	1.97	
363700	1.60	2567	1.06	2767			2.00	1.05
363900	1.70	3910	0.96	3225			2.00	0.97
364120	1.80	4456	0.92	3409			1.94	0.94
364380	1.90	5076	0.91	3544			1.86	0.93
364960	2.00	8304	1.07	3699			1.76	1.12

to wavelength-dispersed infrared interferometry. A sample of three lines from one of these tables is given in Table 9. In order to use these models to compare to a specific observation, integration over a filter profile  $F(\lambda)$  is required:

$$L_F = \int_{\lambda} L(\lambda) d\lambda \quad (2)$$

$$I_F(x) = \int_{\lambda} F(\lambda) I_0(\lambda) f(x, \lambda) d\lambda. \quad (3)$$

Here  $L_F$  is the stellar luminosity as seen through the filter,  $I_F(x)$  is the intensity profile seen through the filter,  $I_0(\lambda)$  are the tabulated values of the central intensity and  $f(x, \lambda)$  are the tabulated values of the normalized CLVs. It is much more preferable to use realistic filter profiles  $F(\lambda)$  with smooth edges (e.g. a Gaussian) rather than square-edged filters in order to minimize noise due to the opacity sampling. Interferometric visibilities can then be obtained from the Hankel transform of  $I_F(x)$ .

<sup>1</sup> <http://www.physics.mq.edu.au/~mireland/codex/>

**Table 6.** Parameters of the compact two cycles of the R52 series, including the position of the shock fronts.

Model	Phase	$L$ ( $L_{\odot}$ )	$R$ ( $R_p$ )	$T_{\text{eff}}$ (K)	S1 ( $R_p$ )	S2 ( $R_p$ )	S3 ( $R_p$ )	S4 ( $R_p$ )
386260	2.36	4640	1.35	2836	2.18			
386280	2.49	3813	1.26	2796	2.56			
386320	2.60	2569	1.13	2680	2.89	1.10		
386500	2.70	3753	0.99	3148	3.09	1.00		
386660	2.80	4198	0.93	3332	3.27	0.95		
386840	2.90	4680	0.90	3486	3.46	0.92		
387040	3.00	8026	0.99	3801		1.02		
387260	3.10	7704	1.18	3446		1.27		
387420	3.19	6844	1.30	3193		1.49		
387580	3.30	5449	1.36	2951		1.70		
387700	3.40	4350	1.34	2805		1.85		
387780	3.49	3585	1.27	2743		1.93		
387860	3.61	2049	1.24	2421		1.98	1.09	
388040	3.70	3560	0.99	3111		1.97	0.99	
388240	3.80	4311	0.93	3355		1.92	0.95	
388480	3.90	4704	0.90	3483		1.83	0.93	
388900	4.00	8166	0.99	3814		1.69	1.03	
389540	4.10	7818	1.17	3473		1.48	1.30	
389680	4.20	6744	1.31	3172		⇒	1.69	
389720	4.32	5120	1.35	2908			2.06	
389740	4.49	3819	1.26	2803			2.45	
389780	4.60	2700	1.12	2728			2.65	1.10
389940	4.69	3700	0.99	3128			2.77	1.00
390120	4.80	4182	0.93	3332			2.88	0.95
390300	4.90	4674	0.90	3482			3.01	0.93

### 3 MODEL SPECTRA

The spectra computed in the CODEX models using the default wavelength table come from an opacity-sampling method with a spectral resolution of up to  $\sim 10^4$ . However, in order to accurately compare with observations at any wavelength, at least  $\sim 100$  wavelengths have to be averaged together, preferably using a non-square edged filter. In turn, this means that these default model outputs can only be used at a spectral resolution of  $R \sim 100$  or lower. This is especially true where the CO bands in  $H$  and  $K$  bands are concerned, where there is a combination of very strong absorption and near-continuum spectral features.

For the purposes of comparing spectra with observations in  $H$  and  $K$  bands, we therefore also computed spectra and CLVs at  $R \approx 10^5$  in these bands. In Figs 9 and 10 we convolved the model spectra with a Gaussian of full width at half maximum (FWHM) equivalent to a spectral resolution of  $R = 1000$ , and compared the model spectra with observations of the Mira variable R Cha from Lançon & Wood (2000). We chose to compare with the o54 series, because the parameters of R Cha are most like those of  $\alpha$  Cet. There was an arbitrary scaling applied to the observed spectra. These scaling factors differed by 0.05 mag between the  $H$  and  $K$  bands for the phase 0.1 spectrum and 0.15 mag for the phase 0.3 spectrum. The best model fits were from phases 0.3 and 0.6, where temperatures were  $\sim 500$  K cooler than phases applicable to the R Cha observations. This demonstrates that in the CO overtone bands, the models are too hot for R Cha. To make this statement more quantitatively based on spectral synthesis, metallicity effects would have to be considered also (beyond the scope of this paper).

### 4 OBSERVATION AND MODEL COMPARISON: $\alpha$ CET

The grand total of all available observations for Mira variables with parameters similar to those of the model series presented here is far too vast to compare to the model series of this paper in a concise manner. Therefore, we have chosen to examine the available observations of  $\alpha$  Cet in a general sense to describe the similarities and differences between the o54 series and  $\alpha$  Cet to further illustrate the utility of the model series and the wealth of information available to constrain models.

Table 10 summarizes most of the key observations available for  $\alpha$  Cet. Time-dependent photometry is available between ultraviolet and radio wavelengths, with the best light curves available in the  $V$ ,  $J$ ,  $H$  and  $K$  bands, as shown in Fig. 5 ( $V$ ,  $J$ ,  $K$ ). There is reasonable agreement between the model and observations for light-curve shape, amplitude and visible-infrared phase offsets.

Spectral classification should also give an observed effective temperature. Unfortunately, the Morgan and Keenan (MK) spectral classification (e.g. Keenan, Garrison & Deutsch 1974) is based on  $B$  and  $V$  bands, where non-LTE effects in an extended atmosphere are very strong (Paper I). Consequently, the combination of effective temperature and metallicity cannot be directly fit to observations. Spectra of  $\alpha$  Cet are also not available electronically to the knowledge of the authors – a modern library of bright Mira spectra would certainly be of great use to future modelling efforts. In particular, infrared spectra are a much more reliable model output, and phase-dependent infrared spectra would be a wonderful tool for tuning model parameters.

Resolved observations have been made at wavelengths between 346 nm and 7  $\mu$ m, with the broad range of highly wavelength-dependent diameters being consistent with models. The form of angular diameter versus wavelength curve as shown in Woodruff et al. (2009) between 1 and 4  $\mu$ m was very similar to the o54 model series; however, in that paper, the models were placed at a distance that best fits the angular diameters. If instead the models are placed at the distance that best fits the  $K$ -band photometry, the angular diameters as a function of phase are given in Figs 11–13. It is clear that the mean diameter of the models is too small, and that the phase dependence of the observed diameter is less pronounced than in the model. Possible solutions to this are given in Sections 5 and 7.

In the radio, the measured angular size of  $\alpha$  Cet corresponds to the angular size of the Na and/or K ionization edges. The consistency between models and observations shows that local thermal equilibrium is a reasonable assumption for defining the ionization fraction. In the ultraviolet, the measured FWHM of 35 mas, corresponding to a shell uniform disc diameter of  $\sim 56$  mas, will provide a strong constraint on the radii of small dust grains. However, model outputs are not currently available for that wavelength range.

### 5 PREDICTING FUNDAMENTAL PARAMETERS WITH MODELS AND OBSERVATIONS

For each Mira variable modelled in this paper, there are currently three physical ( $M$ ,  $L$  and  $Z$ ) parameters and two model parameters ( $\alpha_m$  and  $\alpha_v$ ). In the parameter neighbourhood of the o54 series, we find that the radius of the ‘parent’ star approximated by linear pulsation is given by

$$\frac{R_*}{216 R_{\odot}} \approx \left( \frac{L_*}{5400 L_{\odot}} \right)^{0.8} \left( \frac{M_*}{1.1 M_{\odot}} \right)^{-0.4} \left( \frac{\alpha_m}{3.5} \right)^{-0.7} \left( \frac{Z}{0.02} \right)^{0.2}, \quad (4)$$

**Table 7.** Parameters of the C50 series, including the position of the shock fronts.

Model	Phase	$L$ ( $L_{\odot}$ )	$R$ ( $R_p$ )	$T_{\text{eff}}$ (K)	S1 ( $R_p$ )	S2 ( $R_p$ )	S3 ( $R_p$ )	S4 ( $R_p$ )	S5 ( $R_p$ )
375360	−1.30	2673	0.92	2532	2.49	0.92			
375490	−1.20	3407	0.85	2810	2.56	0.87			
375630	−1.10	3529	0.80	2924	2.59	0.83			
375780	−1.00	6640	0.87	3271	2.63	0.92			
375920	−0.90	7218	1.03	3077	2.62	1.13			
376050	−0.80	7039	1.16	2883	2.60	1.37			
376160	−0.70	6412	1.23	2738	2.55	1.57			
376260	−0.60	5537	1.24	2627	2.48	1.74			
376330	−0.50	4263	1.21	2493	2.38	1.84			
376380	−0.40	2851	1.10	2357	2.19	1.91			
376470	−0.30	2678	0.92	2543	⇒	1.93	0.92		
376630	−0.20	3392	0.84	2816		1.97	0.87		
376820	−0.10	3595	0.80	2937		1.97	0.82		
377110	0.00	6722	0.88	3261		1.86	0.94		
377490	0.10	7253	1.04	3058		1.75	1.18		
377710	0.20	7037	1.16	2876		⇒	1.53		
377750	0.30	6400	1.23	2735			2.01		
377760	0.40	5465	1.24	2618			2.39		
377770	0.53	3720	1.21	2407			2.83		
377790	0.61	2633	1.18	2233			3.06		
377880	0.70	2883	0.91	2606			3.31	0.91	
378020	0.80	3370	0.84	2823			3.55	0.86	
378160	0.90	3813	0.80	2981			3.76	0.82	
378320	1.00	6750	0.89	3253			3.96	0.93	
378470	1.10	7246	1.06	3035			4.15	1.18	
378570	1.21	6955	1.18	2852			4.34	1.44	
378630	1.31	6250	1.23	2713			4.52	1.65	
378660	1.40	5395	1.24	2610			(4.66)	1.80	
378680	1.49	4166	1.21	2476			(4.80)	1.91	
378710	1.61	2512	1.06	2326			(4.97)	1.97	
378810	1.70	2972	0.90	2631				1.95	0.91
378960	1.80	3380	0.83	2827				1.89	0.86

or in angular units

$$\theta_* \propto d^{0.6} F_*^{0.8} M_*^{-0.4} \alpha_m^{-0.7} \left( \frac{Z}{0.02} \right)^{0.2}, \quad (5)$$

where  $d$  is the distance and  $F$  is the received wavelength-integrated stellar flux. In this section we will only discuss the most direct measurements of effective temperature, derived from near-continuum interferometry and photometry, as spectral fitting in the presence of non-LTE effects (Paper I), metallicity and abundance errors is yet to be demonstrated for extended M giants.

There is no dependence of the radius on  $\alpha_v$ , but there is a small dependence of the period  $P$  on  $\alpha_v$  which we will neglect here. The period, which typically is expressed in terms of mass and radius (the so-called PMR relationship), we will express in terms of our model parameters  $L_*$ ,  $M_*$  and  $\alpha_m$ :

$$\frac{P_{\text{lin}}}{261d} \approx \left( \frac{L_*}{5400 L_{\odot}} \right)^{1.8} \left( \frac{M_*}{1.1 M_{\odot}} \right)^{-1.8} \left( \frac{\alpha_m}{3.5} \right)^{-1.5} \left( \frac{Z}{0.02} \right)^{0.4}, \quad (6)$$

Although these relationships are only approximate and do not hold over a wide range of parameters, they demonstrate the complex interplay between the model input parameters. In principle, a measurement of  $Z$  from spectral synthesis, and measurements of period, amplitude, angular diameter, luminosity and distance are enough to constrain  $M$ ,  $\alpha_m$  and  $\alpha_v$ . However, a 10 per cent distance uncertainty (the best of any nearby Mira) translates into a

20 per cent  $L$  uncertainty, or a 20 per cent mass uncertainty keeping everything else fixed at a given period. The relationships are further complicated by the non-linear pulsation period differing significantly from the linear pulsation period (e.g. Table 1), depending on amplitude.

Consider first the problem of calibrating mass independently of pulsation models. Orbital periods for non-interacting Miras are far too long for combined visual and spectroscopic orbits to obtain dynamical masses due to the large radii of Miras. Clusters form a potential hunting ground for Mira variables where the AGB can be calibrated at a known initial mass (e.g. Lebzelter & Wood 2007), but the final mass of the Mira is a function of the assumed mass-loss history, clusters do not easily provide the same age and metallicity range of Miras as in the field, and a direct radius measurement is not yet possible. Mass can also be estimated from kinematics. This is best done for Miras with kinematics inconsistent with the thick disc or halo. The best example of this for nearby Miras is *o* Cet.

*o* Cet has a ( $U$ ,  $V$ ,  $W$ ) space velocity of (−26, −62, −89) km s<sup>−1</sup> when using the revised *Hipparcos* distance from van Leeuwen (2007). This space velocity is unusually large for a Mira, which is a major reason why the interaction between *o* Cet and the interstellar medium produces such an impressive tail (Martin et al. 2007). Although kinematics are often inconclusive when applied to individual stars, this space velocity falls within the 97 per cent probability contour for thick disc membership according to Reddy,



**Table 8.** Parameters of the C81 series, including the position of the shock fronts.

Model	Phase	$L$ ( $L_{\odot}$ )	$R$ ( $R_p$ )	$T_{\text{eff}}$ (K)	S1 ( $R_p$ )	S2 ( $R_p$ )	S3 ( $R_p$ )	S4 ( $R_p$ )	S5 ( $R_p$ )	S6 ( $R_p$ )
243570	−0.40	3917	1.58	2182	2.74	1.96				
243670	−0.30	3705	1.34	2336	2.40	2.06	0.98			
244000	−0.20	5772	0.87	3235	⇒	2.14	0.87			
244140	−0.10	5133	0.79	3311		2.29	0.79			
244330	0.00	9462	0.81	3811		2.25	0.81			
244700	0.10	12460	1.08	3522		2.21	1.14			
246230	0.20	12120	1.28	3212		2.20	1.49			
246810	0.30	11150	1.40	3015		2.05	1.87			
246910	0.40	8327	1.44	2758		⇒	2.31			
246940	0.52	5324	1.65	2310			2.82			
246960	0.61	4427	1.84	2087			3.07			
247020	0.70	4103	1.63	2175			3.39	1.01		
247280	0.80	5302	0.89	3130			3.67	0.89		
247450	0.90	5184	0.79	3322			3.88	0.79		
247560	1.00	10470					4.13	0.78		
247690	1.10	11640	1.06	3498			4.39	1.08		
247810	1.20	12060	1.27	3228			4.54	1.35		
247900	1.30	10990	1.39	3014			(4.80)	1.60		
247970	1.40	8416	1.44	2769			(4.92)	1.79		
248020	1.50	5748	1.58	2405				1.91		
248060	1.59	4234	1.67	2169				1.99		
248130	1.70	4143	1.41	2341				2.00	1.00	
248430	1.80	5493	0.88	3175				1.96	0.88	
248580	1.90	5250	0.79	3326				1.89	0.79	
248730	2.00	9757	0.79	3882				1.76	0.79	
249030	2.10	12020	1.06	3523				1.59	1.09	
249400	2.20	12350	1.26	3255				⇒	1.41	
249500	2.30	11070	1.38	3029					1.82	
249580	2.39	8557	1.42	2801					2.09	
249710	2.50	5655	1.57	2400					2.35	
249890	2.60	4468	1.68	2191					2.53	
250020	2.70	3955	1.59	2180					2.68	1.00
250290	2.80	5609	0.89	3178					2.79	0.89
250440	2.89	5270	0.80	3311					2.88	0.81
250550	3.00	9899							2.94	0.79
250670	3.10	11740	1.06	3501					2.97	1.09
250780	3.20	11920	1.27	3217					2.98	1.36
250870	3.30	10810	1.38	3012					2.98	1.57
250960	3.40	8299	1.43	2765					2.95	1.73
251040	3.49	5758	1.55	2429					2.87	1.84

**Table 9.** An excerpt of the table available online (see Supporting Information) describing the model output for the o54 series model 285180. The CLV is shown as a fraction of the central intensity  $I_0$  as a function of normalized radius on the apparent stellar disc,  $r/5R_p$ .

Wavelength ( $\mu\text{m}$ )	$L_{\lambda}$ ( $\text{erg s}^{-1} \mu\text{m}^{-1}$ )	$I_0$ ( $\text{erg s}^{-1} \text{cm}^{-2} \mu\text{m}^{-1} \text{sr}^{-1}$ )	0.020	CLV: 0.100	$r/5R_p$ 0.140	and 0.170	$I/I_0$ 0.190	0.220	0.290	0.360	0.440
1.598	0.9786E+37	0.1124E+10	0.997	0.923	0.828	0.691	0.451	0.082	0.066	0.053	0.046
1.599	0.8160E+37	0.3054E+09	0.999	0.977	0.955	0.932	0.913	0.879	0.796	0.662	0.337
1.600	0.1106E+38	0.1427E+10	0.998	0.940	0.863	0.743	0.274	0.024	0.022	0.022	0.026

Lambert & Allende Prieto (2006). In the detailed analysis of Robin et al. (2003), the  $W$  velocity of *o* Cet is inconsistent at  $5\sigma$  with even the old (5–10 Gyr) thin disc, and is most consistent with being a member of the thick disc, modelled as a single stellar population of 11 Gyr age. Importantly, *o* Cet cannot be a runaway star (e.g. Hoogerwerf, de Bruijne & de Zeeuw 2000) where its space velocity is due to a single strong gravitational interaction in its past, because it has retained its wide companion Mira B, and the orbit cannot be highly eccentric as the periastron must be outside the atmosphere

of *o* Cet. Therefore, the progenitor mass of *o* Cet is almost certainly less than  $1.1 M_{\odot}$  [e.g. the Girardi et al. (2000) evolutionary tracks place a  $1.06 M_{\odot}$  star on the TP-AGB after 10 Gyr, or less for sub-solar metallicity]. This places the current mass of *o* Cet at  $1 M_{\odot}$  or less. This is close to our model value of  $1.1 M_{\odot}$ . However, if  $L$  were to be kept constant and  $M$  decreased,  $\alpha_m$  would have to be increased further from its already large value in order to maintain the period. We will discuss this further below after first discussing  $\alpha_m$ .

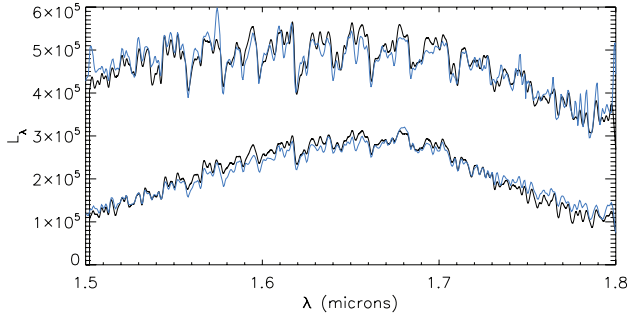


**Figure 9.** A *H*-band comparison of the R Cha spectrum at phases 0.1 (top) and 0.3 (bottom) to the 287820 (top) and 250460 (bottom) models of the o54 series.

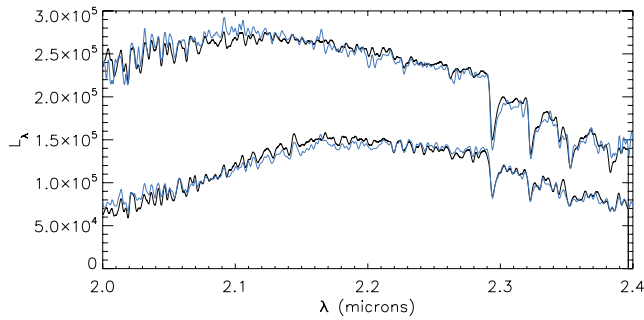


**Figure 10.** A *K*-band comparison of the R Cha spectrum at phases 0.1 (top) and 0.3 (bottom) to the 287820 (top) and 250460 (bottom) models of the o54 series.

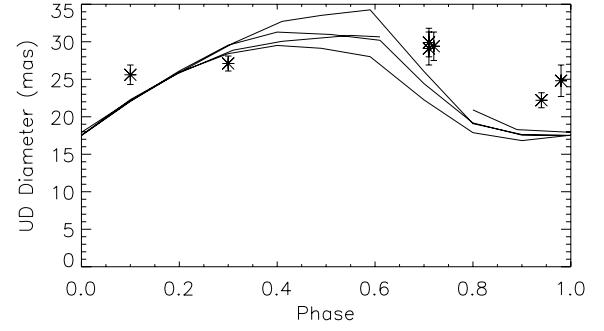


**Figure 11.** Model diameters of the o54 series in a narrow 1.24  $\mu\text{m}$  bandpass based on fitting to a single spatial frequency where  $V = 0.6$ , with the measured diameters from Woodruff et al. (2008) overplotted.

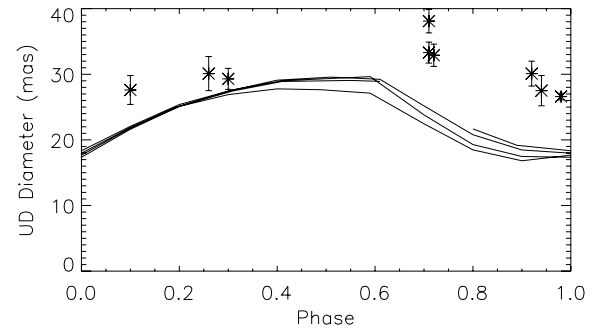


**Figure 12.** The same as Fig. 11, except for the *H* band.

**Table 10.** Summary of key observational data on *o* Cet. Units: Vega magnitudes for light curves, mJy for radio photometry and milliarcsec for diameters.

Wavelength ( $\mu\text{m}$ )	Data type	Observation range	Model range	Phase coverage?	References
0.55	Light curve	2.5–9.5	2.0–11	Y	AFOEV
1.2	Light curve	(−1.7) to (−0.3)	(−1.8) to (−0.6)	Y	Whitelock et al. (2000)
1.65	Light curve	(−2.6) to (−1.3)	(−2.6) to (−1.5)	Y	Whitelock et al. (2000)
2.2	Light curve	(−3.0) to (−1.8)	(−3.0) to (−2.0) <sup>c</sup>	Y	Whitelock et al. (2000)
0.4–0.6	Spectral type	M5e to M9e	None <sup>b</sup>	Y	Skiff (2009); Samus et al. (2004)
0.307	Photometry	14.85	None <sup>e</sup>	N	Karovska et al. (1997)
0.346	Diameter	35 (FWHM)	None <sup>b</sup>	N	Karovska et al. (1997)
0.45–1.03	Diameter	31–103	25–60 <sup>d</sup>	N	Labeyrie et al. (1977)
0.68–0.92	Diameter	20–60 FWHM	16–38	N	Ireland et al. (2004)
1.24	Diameter	22–30	17–34	Y	Woodruff et al. (2008)
2.26	Diameter	31–37	17–29	Y	Woodruff et al. (2008)
1.24	Diameter	22–30	17–32	Y	Woodruff et al. (2008)
1.1–3.8	Diameter	25–68	17–58	N	Woodruff et al. (2009)
11.15	Diameter	46–55	21–72	Y	Weiner, Hale & Townes (2003)
3.6 cm <sup>a</sup>	Photometry	0.20–0.37 mJy	0.09–0.32 mJy	N	Reid & Menten (1997); Matthews & Karovska (2006)
7 mm	Diameter	52	29–55	N	Reid & Menten (2007)

<sup>a</sup>Shorter-wavelength radio observations are consistent with a  $\nu^2$  power law within errors. A 0.12 mJy contribution from Mira B has been subtracted.

<sup>b</sup>No model spectral-type calculations are possible (see text).

<sup>c</sup>Distance to model fixed to 107 pc so that *K*-band maximum agrees.

<sup>d</sup>When the fluorescence scattering approximation is used (as in Paper I), the range becomes 26–80 mas, with the upper diameter limited by the model  $5R_p$  surface.

<sup>e</sup>Although the ultraviolet is important for deep-atmosphere temperature profiles, no ultraviolet fluxes are output because the near-surface opacities are likely unreliable.

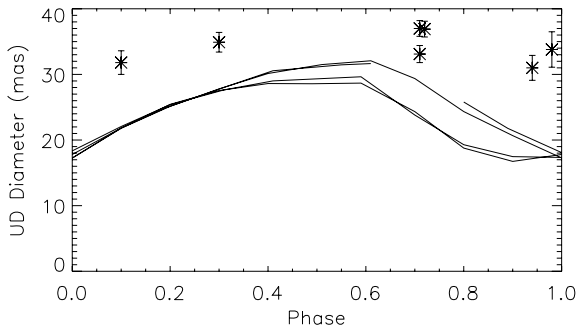


**Figure 13.** The same as Fig. 11, except for the *K* band.

The comparisons of models to observations in this paper have already provided significant evidence that model temperatures are too high, implying that  $\alpha_m = 3.5$  is too high a value for Miras with parameter ranges applicable to *o* Cet and R Cas. There are three key pieces of evidence: the near-maximum *V* – *K* colours, the infrared spectral fitting for R Cha and the measured angular diameters.

All series with  $\alpha_m = 3.5$  are too warm near maximum, as shown by their *V* – *K* colours of  $<5.0$ . The R52 and C81 series compared to R Leo and R Cas, respectively, are the most discrepant. Although in general this could be due to fundamental parameters  $M$  and  $L$  only, in this case it is not possible. The R Cas R81  $1.35 M_\odot$ ,  $8160 L_\odot$  model is reasonable for a Mira: i.e. all AGB stars above a certain mass will go through an  $8160 L_\odot$  phase, and the mass of  $1.35 M_\odot$  at  $8160 L_\odot$  will result from some initial mass. The systematic study of Mira spectral type at maximum by Keenan et al. (1974) found a trend of systematically later spectral types with increasing Mira period, with no Miras having near-maximum spectral types earlier than M5 in the 350–500 d period range. The model spectral type of  $\sim M2$  for R Cas is therefore much too warm. This means that the combined choice of  $\alpha_m = 3.5$  and  $\alpha_v = 0.32$  together is incorrect for stars in the vicinity of  $M = 1.35 M_\odot$  and  $L = 8160 L_\odot$ .

R Cha is a Mira variable very much like *o* Cet (period, amplitude, colour), except for its more uncertain distance. In Section 3, we saw that the models were  $\sim 500$  K too hot for R Cha. However, R Cha has the hottest near-maximum spectral type of all Mira variables at periods of  $\sim 300$ – $350$  d in Keenan et al. (1974), so this suggests that the models are too hot for any Mira. Inspection of some low-metallicity test models (to be published) indicates that decreasing the metallicity reduces this discrepancy but does not remove it.

Although the range of model diameters reported by Woodruff et al. (2008) were roughly consistent with the range of diameters for the Miras studied in that paper, the minimum measured diameter for each star was larger than the minimum diameter predicted by models. This remains true for the current model series (see Section 4), especially for *o* Cet. A discrepancy in near-continuum diameters at phases  $\sim 0.9$ – $0.2$ , where the photosphere is relatively compact, can only be rectified with an increase in model radius by 10–20 per cent.

Let us consider how models of *o* Cet could be modified in order to achieve a larger apparent radius. The simplest method is to place the star at a closer distance with a lower luminosity and the same linear radius and mass (preserving the period). We note that the most recent *Hipparcos* analysis of van Leeuwen (2007) places *o* Cet as close as 75 pc within  $2\sigma$ , which would mean luminosities as low as  $2650 L_\odot$  are consistent with direct observations. Such a low luminosity would, however, be 0.8 mag below the LMC P-L relationship (Whitelock et al. 2008). This relationship provides a stronger constraint on the absolute *K*-magnitude of *o* Cet, as the

dispersion in the relationship is only 0.13 mag (Feast et al. 1989). Adopting this relationship places a  $2\sigma$  lower limit on the *o* Cet luminosity of  $4400 L_\odot$ . By solving the approximate equations (4) through (6) after decreasing the  $M$  to  $1 M_\odot$  and increasing angular diameter by 10 per cent, the model luminosity becomes  $4200 L_\odot$  and the mixing-length parameter  $\alpha_m = 2.9$  (effects of  $\alpha_v$  and  $Z$  are neglected here). It is therefore likely not possible to fit all observations of *o* Cet unless the model mass is greater than  $1 M_\odot$  or the luminosity more than  $2\sigma$  below the LMC P-L relationship – each of which would be a controversial claim. This discussion shows just how difficult it is to provide precisely calibrated models of Mira variables without clear observational reference points.

The key problem here of finding the best value for  $\alpha_m$  as a function of  $M$  and  $L$  can be expressed as a problem of finding the radii of real stars at given  $M$  and  $L$ . Mixing length only provides a way to calculate  $R$  for given  $M$  and  $L$  once free parameters (especially the mixing length) are fixed based on known stars. Models of main-sequence stars and even K giants can be calibrated very well from the Sun and other stars of accurately known parallax. However, extrapolating to M giants, where pressure scaleheights can be a significant fraction of a radius, is not expected to be reliable.

What is therefore needed is a sample of M giants of well-known  $M$ ,  $L$  and  $R$ , from which to calibrate the mixing length. Although we cannot measure  $M$ , period can serve as a proxy for  $M$  given  $L$  and  $R$ .  $L$  and  $R$  can be measured accurately for a sample of stars with relatively compact atmospheres (i.e. with a well-defined  $R$ ) that have a well-known parallax, photometry and effective temperature. At this point, spectral synthesis is not reliable enough or calibrated well enough for M giants to produce accurate effective temperatures and compositions. Therefore, this sample should include semi-regular pulsators with accurate photometry, angular diameters and periods. Either accurate periods or angular diameters are currently missing for many of the closest M giants, so we suggest that measuring and collating such information should be an active area of research.

Assuming that a reasonable value for  $\alpha_m$  can be prescribed for Mira models, the main free parameters for any individual Mira are composition and  $\alpha_v$ . Composition (primordial metallicity and C/O ratio) must come from the spectral synthesis. Given a set of Miras with well-measured distances,  $L$  is determined from observations and  $M$  from the period of the Mira – only  $\alpha_v$  can be used to tune the model amplitude and should be relatively easy to calibrate.

## 6 THE MOLECULAR-SHELL SCENARIO

Interferometric measurements of Mira variables have been shown to be internally consistent only if there is a layer of molecular water far above the continuum-forming photosphere (e.g. Weiner 2004). Observational comparison with models that include this kind of water and/or dust layer has so far been dominated by non-physical models, i.e. those that neither provide a mechanism for elevating the emitting material nor provide calculations of the chemistry that determines which components dominate the radiative transfer at which radii.

Nevertheless, these ad hoc models have provided a relatively simple picture for the regions around Mira variables and have impressively fitted a limited selection of observable properties. In this section we will examine the physical and observable properties of the molecular shells in our model series.

Figs 1–4 show that cycle-to-cycle variations in the pulsation models are generally quite modest in terms of the luminosity, of the temperature at and the position of the  $\tau_g = 2/3$  layer and of the

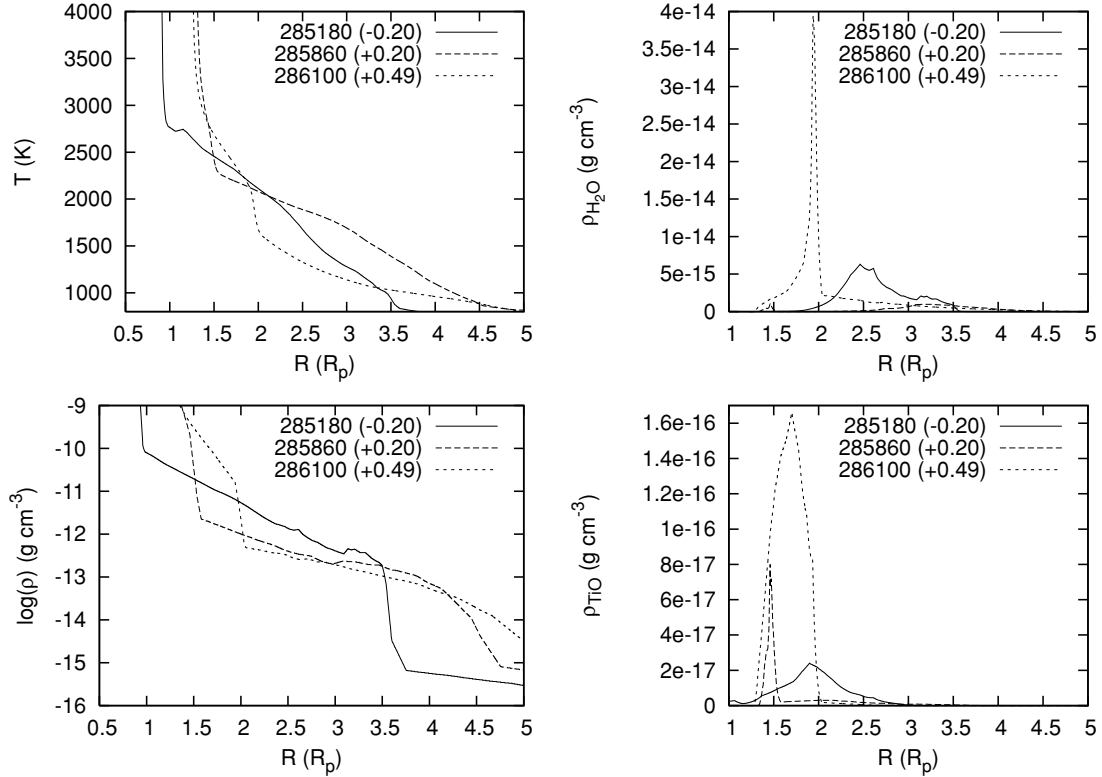


**Figure 14.** Temperature (K ; upper left), density ( $\text{g cm}^{-3}$  ; lower left panel) and the molecular density  $\rho_{\text{mol}}$  for molecules  $\text{H}_2\text{O}$  (upper right) and  $\text{TiO}$  (lower right) as a function of  $r/R_p$  for three phases of a cycle of the o54 model series: 285180 (phase  $-0.20$ , solid line), 285860 ( $+0.20$ , dashed) and 286100 ( $+0.49$ , short-dashed).

position of deep-layer mass zones below the  $\tau_g = 2/3$  layer. The o54 and C81 model series show somewhat more pronounced cycle-to-cycle effects than the R52 and C50 models. Inspection of specific numerical values of the radius  $R$  of the  $\tau_{\text{Ross}} = 1$  layer and the therefrom derived effective temperature  $T_{\text{eff}} \propto (L/R^2)^{1/4}$  given in Tables 2–8 for the non-grey atmospheric stratifications confirms this cycle stability.

In contrast, we notice substantial differences between different cycles, and often between successive cycles, in terms of the positions of high-layer mass zones (Figs 1–4). These differences are closely related to substantial differences of the strengths and positions of outwards travelling shock fronts. Inspection of shock-front positions (Tables 2–8) in the selected cycles for which detailed atmospheric models were computed shows a shock front typically emerging at pre-maximum phase around  $-0.3$  to  $-0.1$ , then travelling outwards during about 1 to 1.5 cycles while it becomes weaker and slower before the subsequent front catches up and both fronts merge. Typically, the outer front starts retreating before merger, but occasional shock fronts travelling towards circumstellar space (where they eventually fade away) are also seen in the tables.

The positions and heights of shock fronts at different phases and in different cycles determine the upper atmospheric density stratification and, therefrom, the details of the temperature stratification and of the partial-pressure stratification of molecular absorbers. The assumptions of local thermodynamic equilibrium and spherical symmetry are sufficient to derive this stratification [as may not be the case for the so-called MOLsphere (Tsuji 2000) in supergiants, due to the co-existence of the chromosphere in those stars]. The study of Tej, Lançon & Scholz (2003), based on models of

Hofmann et al. (1998), shows that the details of shock-front propagation may lead to strong cycle-to-cycle differences of the stratification of the outer atmosphere resulting in strong differences of the density and geometric characteristics of water ‘shells’, i.e. of layers whose absorption is dominated by water molecules.

Figs 14–16 demonstrate, for the o54 and the r50 series of the here presented CODEX model sets, the drastic phase and cycle effects of shock-front propagation on the temperature–density stratification and on the appearance of  $\text{H}_2\text{O}$  and  $\text{TiO}$  ‘shells’. Density decreases monotonically with radius, while the sharp decrease at a shock front provides the *outer* edge of any ‘shell’. The decrease of temperature with radius provides a relatively sharp edge to the region where water can exist in chemical equilibrium, and this provides the *inner* edge of any ‘shell’. At most infrared wavelengths, gas is reasonably transparent between temperatures where  $\text{H}^-$  opacity is dominant ( $\gtrsim 3000$  K) and where water is dominant ( $\lesssim 1800$  K). A similar pattern is found for the  $\text{TiO}$  molecule which, however, is formed in somewhat deeper layers than water and, therefore, does not depend so strongly on upper-atmosphere shock fronts and shows smaller, though by no means negligible, cycle-to-cycle effects.

The model-predicted effects of such molecular ‘shells’ upon the absorption properties of the stellar atmosphere at observationally important wavelengths have been discussed and compared to observations by Paper I, Woodruff et al. (2009) and Wittkowski et al. (2011). Fig. 17 shows typical cycle-to-cycle differences seen in the water-contaminated spectrum of the three models presented in Fig. 15. Typical effects of water ‘shells’ upon the shape of the CLV have been discussed in the model study of Tej et al. (2003).

Though semi-empirical ‘shell’ scenarios have been used with remarkable success for interpreting spectroscopic and interferometric



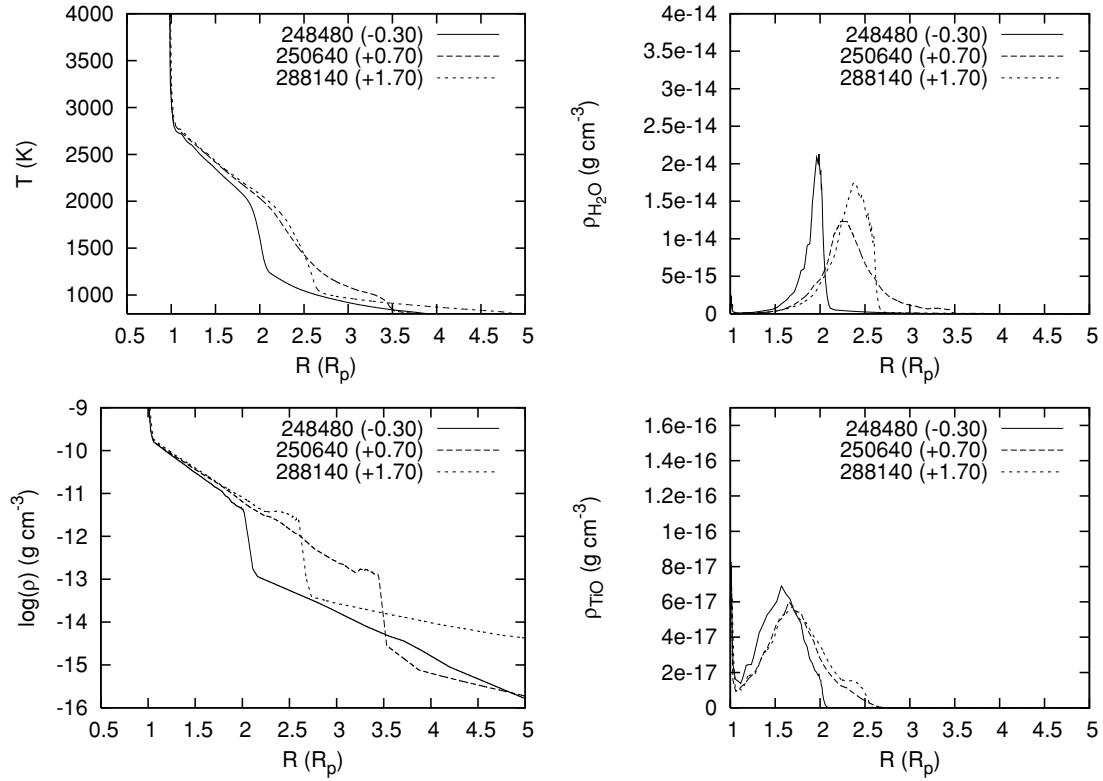


**Figure 15.** The same as Fig. 14 for the same phase 0.7 of three models of different cycles of the o54 model series: 248480 ('extended' series  $-0.30$ , solid line), 250640 ('extended' series  $+0.70$ , dashed) and 288140 ( $+1.70$ , short-dashed).

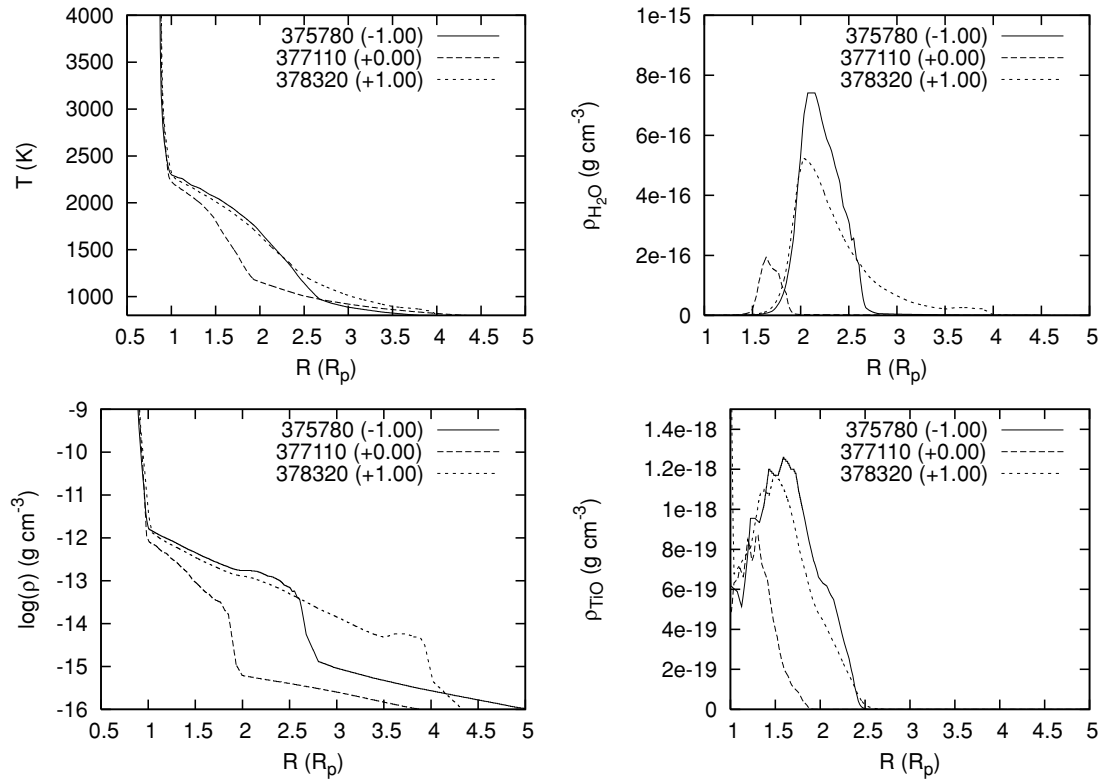


**Figure 16.** The same as Fig. 14 for the same phase 0.0 of three models of successive cycles of the r50 model series: 375780 ( $-1.00$ , solid line), 377110 ( $0.00$ , dashed) and 3783200 ( $+1.00$ , short-dashed).

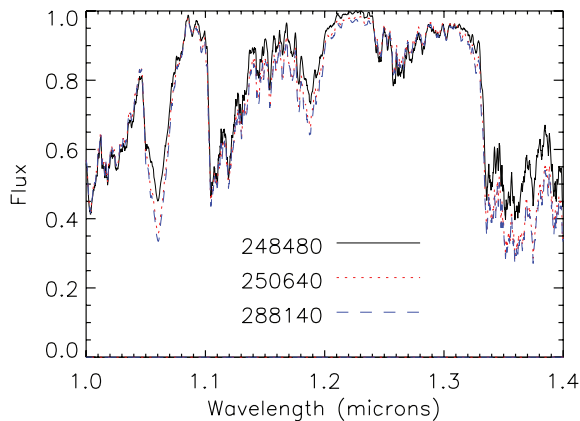


**Figure 17.** Spectra of the three same-phase models of Fig. 15 showing cycle-to-cycle differences of the spectrum in the *J*-band region of the spectrum.

observations of absorption features of H<sub>2</sub>O (e.g. Matsuura et al. 2002; Mennesson et al. 2002; Ohnaka 2004; Perrin et al. 2004; Weiner 2004) and of TiO (e.g. Reid & Goldston 2002), models show that such scenarios can at best provide a very rough picture of the approximate instantaneous position and extent of absorbing layers. Such semi-empirical models cannot provide any information on changes of these layers with phase [since local molecule abundance and resulting molecule absorption as a function of local values of  $\rho(r)$  and  $T(r)$  sensitively depend on details of shock-front progression]. Note also that absorption by CO in low excitation lines extends from the continuum-forming photosphere at  $\sim 3000$  K right to the wind region, so a CO ‘shell’ scenario (e.g. Mennesson et al. 2002) should be considered with particular caution.

Finally, we note that the existence of shell-like structures noticeably changes the computed spectra in the models, but the effects are not so strong that the detailed shell structure can be directly inferred from low spectral resolution observations. Modelling high spectral resolution observations is beyond the scope of this paper, but such a study would have to take into account the velocity structure of the atmosphere explicitly (e.g. Nowotny, Höfner & Aringer 2010).

## 7 RADIATIVE ACCELERATION AND MASS LOSS

As described in Höfner (2008), the conditions for radiative acceleration to drive mass loss are that dust must be able to form, and that the opacity exceeds the critical opacity:

$$\kappa > \frac{4\pi c G M_*}{L_*} = 12\,830 \text{ cm}^2 \text{ g}^{-1} \left( \frac{M_*}{M_\odot} \right) \left( \frac{L_*}{L_\odot} \right)^{-1}. \quad (7)$$

This opacity is attainable at solar metallicity with fully condensed iron-rich dust, which is not stable until approximately 5 continuum stellar radii (Woitke 2006). This opacity is also reached by forsterite (i.e. Fe-poor silicate) grains of 400 nm radius due to strong scattering (Höfner 2008).

The CODEX models have a chemical equilibrium model of dust formation, so are not appropriate for modelling the slowly growing Fe-rich dust at  $\lesssim 5 R_p$ , and indeed we artificially cut-off Si condensation at a condensation fraction of 0.25 for this reason. However, as discussed in Ireland & Scholz (2006), the prescription we use for dust formation is reasonably accurate for Fe-poor silicates.

The strongest observational constraints on the radii of dominant dust species are observations that probe the opacity at short

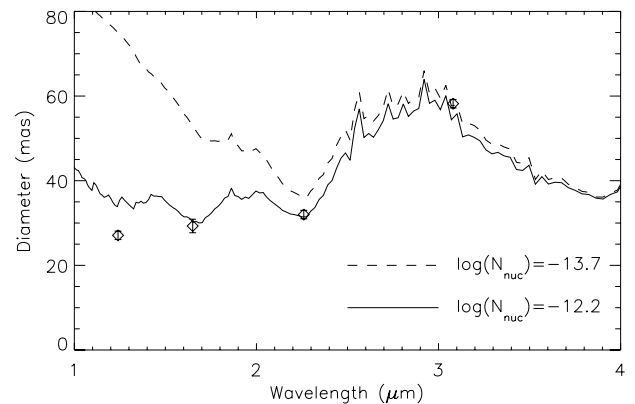


**Figure 18.** Interferometric diameters for the o54 series model 286060 (phase 0.41), fit to the spatial frequency where visibility  $V = 0.5$ . The solid line corresponds to the default number of dust nuclei, and the solid red line corresponds to a factor of 3.1 increase in grain radius, at  $\log(N_{\text{nuc}}) = -13.7$ . Observations from Woodruff et al. (2008) at phase 0.3 are overplotted. Despite still not being able to drive a wind, the large diameters at short wavelengths are clearly inconsistent with observations.

wavelengths where dust scattering is dominant, and wavelengths where water absorption is dominant. As optically thin scattering does not affect the spectrum, the best observations to probe this difference are resolved observations of Miras as a function of wavelength. Fig. 18 shows the interferometric diameters of *o* Cet as a function of wavelength as measured by Woodruff et al. (2008) along with the diameters predicted by the 286060 model and the diameters predicted by the same model with the base-10 logarithm of the number of dust nuclei per H atom  $N_{\text{nuc}}$  decreased from  $-12.2$  to  $-13.7$ , and the corresponding maximum grain radius increased from 63 to 194 nm. These large grains still have insufficient opacity to overcome gravity in this model. We could not increase the grain radii further without the optical depths becoming too large at our chosen  $5R_p$  surface, and the preferred value from Höfner (2008) of  $\log(N_{\text{nuc}}) = -15$  would produce diameters that are far too large. It is clear that these large grain radii are not consistent with the relatively large H<sub>2</sub>O column densities at several continuum radii inferred from infrared interferometric observations. Either radiation pressure on small Fe-rich grains or large Fe-poor grains could drive winds from M-type Mira variables, but the base of the wind and the grains that drive it must originate from layers higher than where H<sub>2</sub>O is seen in the near-infrared, i.e. higher than about 3 continuum-forming radii.

## 8 CONCLUSIONS AND FUTURE WORK

The atmospheric models presented here, based on self-excited pulsation models and opacity-sampling treatment of radiation transport, provide a fairly realistic approximation of the atmospheric density–temperature stratification. Many spectral features are predicted with satisfactory accuracy but some, like TiO bands, require further improvement of the models e.g. the non-LTE treatment of Paper I. The present sequence of models also comprises only four combinations of basic stellar parameters at only a single composition and, therefore, can only describe a relatively small subset of Mira variables. Predictions of the four model series presented here (Table 1) are available online (Section 2.5).

There are several potential causes of substantial deviation from spherical asymmetry in Mira variables – including convective

cells, weak chaos and Rayleigh–Taylor instabilities (Woitke 2006). Asymmetries are clearly not considered in our model series as they are spherically symmetric, but asymmetries are relatively common in Mira variables when observed at sufficient angular resolution (e.g. Ragland et al. 2006). The one prediction that can be made from the models is that the wavelengths most susceptible to cycle-to-cycle variations (e.g.  $L$  band where the water shells are optically thick) should also show asymmetries, as high layers on opposite sides of the star should not be strongly causally connected and show weak chaos. We finally suggest that an observation so far missing in the literature is the astrometric motions of the radio photosphere over several cycles, which should be a strong indicator for the degree of high-layer chaos in Mira atmospheres.

Determination of the internal fundamental model parameters, i.e. mixing-length  $\alpha_m$  and turbulent viscosity  $\alpha_v$  (Table 1), would require the observation of a set of stars with different mass, luminosity and pulsation period. For a given pulsation period, a higher-mass star must have a higher luminosity (radius), but a similar effective temperature. We suggest that further studies of low-amplitude pulsators with Mira-like periods such as R Dor and W Hya may provide the key to tuning the mixing-length parameter  $\alpha_m$  of Mira model series. These are likely higher-mass stars, but with a similar effective temperatures to  $\alpha$  Cen. Tuning the turbulent viscosity parameter will best be done by fitting to amplitudes of models with the best-known masses such as, e.g., those kinematically associated with the thick disc.

## ACKNOWLEDGMENTS

MJI would like to acknowledge support from the Australian Research Council through an Australian Postdoctoral Fellowship. PRW was partially supported by Australia Research Council grant DP1095368. We acknowledge with thanks the variable star observations from the AAVSO International Data base contributed by observers worldwide and used in this research. This research has made use of the AFOEV data base, operated at CDS, France.

## REFERENCES

- Edvardsson B., Andersen J., Gustafsson B., Lambert D. L., Nissen P. E., Tomkin J., 1993, *A&A*, 275, 101  
 Feast M. W., Glass I. S., Whitelock P. A., Catchpole R. M., 1989, *MNRAS*, 241, 375  
 Fluks M. A., Plez B., The P. S., de Winter D., Westerlund B. E., Steenman H. C., 1994, *A&AS*, 105, 311  
 Gail H.-P., 2003, in Henning Th., ed., *Lect. Notes Phys.* Vol. 609, *Astromineralogy*. Springer, Berlin, p. 55  
 Girardi L., Bressan A., Bertelli G., Chiosi C., 2000, *A&AS*, 141, 371  
 Grevesse N., Noels A., Sauval A. J., 1996, in Holt S. S., Sonneborn G., eds, *ASP Conf. Ser.* Vol. 99, *Cosmic Abundances*. Astron. Soc. Pac., San Francisco, p. 117  
 Hofmann K.-H., Scholz M., Wood P. R., 1998, *A&A*, 339, 846  
 Höfner S., 2008, *A&A*, 491, L1  
 Höfner S., Jørgensen U. G., Loidl R., Aringer B., 1998, *A&A*, 340, 497  
 Höfner S., Gautschi-Loidl R., Aringer B., Jørgensen U. G., 2003, *A&A*, 399, 589  
 Hoogerwerf R., de Bruijne J. H. J., de Zeeuw P. T., 2000, *ApJ*, 544, L133  
 Hughes S. M. G., Wood P. R., 1990, *AJ*, 99, 784

- Ireland M. J., Scholz M., 2006, *MNRAS*, 367, 1585  
 Ireland M. J., Tuthill P. G., Bedding T. R., Robertson J. G., Jacob A. P., 2004, *MNRAS*, 350, 365  
 Ireland M. J., Scholz M., Wood P. R., 2008, *MNRAS*, 391, 1994 (Paper I)  
 Jura M., Kleinmann S. G., 1992, *ApJS*, 79, 105  
 Karovska M., Hack W., Raymond J., Guinan E., 1997, *ApJ*, 482, L175  
 Keenan P. C., Garrison R. F., Deutsch A. J., 1974, *ApJS*, 28, 271  
 Knapp G. R., Pourbaix D., Platais I., Jorissen A., 2003, *A&A*, 403, 993  
 Labeyrie A., Koechlin L., Bonneau D., Blazit A., Foy R., 1977, *ApJ*, 218, L75  
 Lançon A., Wood P. R., 2000, *A&AS*, 146, 217  
 Lebzelter T., Wood P. R., 2007, *A&A*, 475, 643  
 Martin D. C. et al., 2007, *Nat*, 448, 780  
 Matsuura M., Yamamura I., Cami J., Onaka T., Murakami H., 2002, *A&A*, 383, 972  
 Matthews L. D., Karovska M., 2006, *ApJ*, 637, L49  
 Meakin C. A., Arnett D., 2007, *ApJ*, 667, 448  
 Mennesson B. et al., 2002, *ApJ*, 579, 446  
 Menzies J. W., Whitelock P. A., Feast M. W., Matsunaga N., 2010, *MNRAS*, 406, 86  
 Nadzhip A. E., Tatarnikov A. M., Shenavrin V. I., Weigelt G., Yudin B. F., 2001, *Astron. Lett.*, 27, 324  
 Nowotny W., Höfner S., Aringer B., 2010, *A&A*, 514, A35  
 Ohnaka K., 2004, *A&A*, 424, 1011  
 Perrin M. D., Graham J. R., Kalas P., Lloyd J. P., Max C. E., Gavel D. T., Pennington D. M., Gates E. L., 2004, *Sci*, 303, 1345  
 Ragland S. et al., 2006, *ApJ*, 652, 650  
 Reddy B. E., Lambert D. L., Allende Prieto C., 2006, *MNRAS*, 367, 1329  
 Reid M. J., Goldston J. E., 2002, *ApJ*, 568, 931  
 Reid M. J., Menten K. M., 1997, *ApJ*, 476, 327  
 Reid M. J., Menten K. M., 2007, *ApJ*, 671, 2068  
 Rejkuba M., 2004, *A&A*, 413, 903  
 Robin A. C., Reylé C., Derrière S., Picaud S., 2003, *A&A*, 409, 523  
 Samus N. N. et al., 2004, *VizieR Online Data Catalog*, 2250  
 Skiff B. A., 2009, *VizieR Online Data Catalog*, 1, 2023  
 Tej A., Lançon A., Scholz M., 2003, *A&A*, 401, 347  
 Tsuji T., 2000, *ApJ*, 540, L99  
 van Leeuwen F., 2007, *Astrophys. Space Sci. Libr.*, Vol. 350, *Hipparcos, the New Reduction of the Raw Data*. Springer, Dordrecht  
 Weiner J., 2004, *ApJ*, 611, L37  
 Weiner J., Hale D. D. S., Townes C. H., 2003, *ApJ*, 588, 1064  
 Whitelock P., Marang F., Feast M., 2000, *MNRAS*, 319, 728  
 Whitelock P. A., Feast M. W., van Leeuwen F., 2008, *MNRAS*, 386, 313  
 Wittkowski M. et al., 2011, *A&A*, 532, 7  
 Woitke P., 2006, *A&A*, 452, 537  
 Woodruff H. C., Tuthill P. G., Monnier J. D., Ireland M. J., Bedding T. R., Lacour S., Danchi W. C., Scholz M., 2008, *ApJ*, 673, 418  
 Woodruff H. C. et al., 2009, *ApJ*, 691, 1328  
 Wyatt S. P., Cahn J. H., 1983, *ApJ*, 275, 225

## SUPPORTING INFORMATION

Additional Supporting Information may be found in the online version of this article:

**Table 9.** The model output for the o54 series model 285180.

Please note: Wiley-Blackwell are not responsible for the content or functionality of any supporting materials supplied by the authors. Any queries (other than missing material) should be directed to the corresponding author for the article.

This paper has been typeset from a  $\text{\LaTeX}$  file prepared by the author.